Journal of Materials Chemistry C

ROYAL SOCIETY OF CHEMISTRY

PAPER

View Article Online
View Journal

Cite this: DOI: 10.1039/d6tc00316h

Role of Ce^{3+} doping in the photochromic and storage properties of $Ca_3MgSi_2O_8$

Guna Krieke, *[ab] Alexei Kuzmin, [b] Inga Pudza, [b] Aleksandr Kalinko, [b] Guna Doke, [ab] Arturs Zarins, [cd] Andris Antuzevics, [b] Aivaras Kareiva [a] and Aleksej Zarkov [a]

Received 30th January 2026,
Accepted 4th March 2026

DOI: 10.1039/d6tc00316h

rsc.li/materials-c

In this study, the role of Ce^{3+} doping in the photochromic, thermostimulated luminescence (TSL), and optically stimulated luminescence (OSL) properties of $Ca_3MgSi_2O_8$ is analyzed. Ce^{3+} was incorporated into the $Ca_3MgSi_2O_8$ lattice using high-temperature solid-state synthesis, and its effects on structure, defect formation, charge trapping, and spectroscopic properties were investigated using X-ray diffraction (XRD), photoluminescence (PL), X-ray absorption spectroscopy, optical absorbance, TSL/OSL, and electron paramagnetic resonance (EPR) measurements. The results indicate that Ce^{3+} primarily substitutes for Ca^{2+} ions at the Ca2 site with distorted eightfold coordination. Ce^{3+} doping enhances photochromic efficiency, reaching up to 88% for UV-induced color change, and influences the formation of defect centers responsible for photochromism and luminescence. TSL and OSL analyses indicate the presence of deep charge traps with an activation energy of 1.79 eV, which can be stimulated using blue light. EPR identifies three distinct F^+-type centers; two of these centers are located in the vicinity of boron impurities, which originate from the borate additive used in the synthesis. The material exhibits excellent photochromic signal stability and a linear TSL dose response up to 40 Gy, suggesting strong potential for dosimetry and optical information storage.

1. Introduction

Photochromic materials are compounds that can undergo a reversible change in their optical absorption or color upon exposure to radiation, such as ultraviolet (UV), visible light, or ionizing radiation.[1–3] Among others, inorganic wide band gap photochromic materials have attracted interest due to superior thermal, chemical, and photochemical stability, excellent fatigue resistance after repeated color change, long operational lifetime, and the ability to integrate photochromism with additional functionalities such as luminescence or sensing.[1,2] As a result, these materials have been proposed for various optical applications, such as optical data storage,[4,5] UV and radiation dosimetry,[6,7] smart windows and adaptive glazing,[8,9] and multilevel anti-counterfeiting.[10,11]

In inorganic wide band gap materials, the typical mechanism of photochromism involves the generation of charge carriers during irradiation, which are trapped in charge traps, where they form point defects with characteristic absorption bands.[2] The efficiency and applicability of these materials depend on their ability to generate, store, and release charge carriers through trapping and recombination processes, which are influenced by synthesis conditions and selected dopants.[12–14] Rare-earth ions are the most commonly used dopants for inorganic photochromic materials,[1] which can both modify the defect concentration through heterovalent substitution in the host lattice and act as charge trap centers.[14–16] In addition, rare-earth dopants can induce other spectroscopic effects, such as modulated photoluminescence (PL), thermostimulated luminescence (TSL), and optically stimulated luminescence (OSL).[13,17–19]

Recently, rare earth doped merwinite ($Ca_3MgSi_2O_8$) has been investigated as an efficient and tunable phosphor,[20–22] a persistent luminescence host,[23–25] a TSL dosimetry material[26] and a highly efficient photochromic host, with one of the highest color contrasts reported to date.[27,28] Although the host matrix itself shows photochromism, it can be considerably improved by doping with Eu^{2+}, which not only enhances photochromic efficiency but also enables UV-modulated PL, TSL with unusually deep charge traps, and OSL response.[27,28] The multimodal nature of $Ca_3MgSi_2O_8$:Eu^{2+} shows the potential of this host for optical information storage, anti-counterfeiting, and dosimetry applications.

[a] Institute of Chemistry, Vilnius University, Naugarduko 24, LT-03225 Vilnius, Lithuania. E-mail: guna.krieke@cfi.lu.lv
[b] Institute of Solid State Physics, University of Latvia, 8 Kengaraga str., LV-1063, Riga, Latvia
[c] University of Latvia, Faculty of Science and Technology, Institute of Chemical Physics, 1 Jelgavas str., LV-1004 Riga, Latvia
[d] Daugavpils University, Faculty of Natural Sciences and Healthcare, Department of Environment and Technologies, 1A Parades str., LV-5401 Daugavpils, Latvia

Despite the promising performance of $Ca_3MgSi_2O_8:Eu^{2+}$, the influence of alternative rare-earth dopants on defect formation, charge trapping, and multimodal optical responses in this host remains unexplored. Currently, Eu^{2+} is the only dopant systematically investigated in photochromic $Ca_3MgSi_2O_8$, where it has been shown to act as a photoionizable hole trap.[27,28] As an alternative, Ce^{3+} is particularly interesting due to its 4f–5d transitions and similar photoionization behavior. The photoionization of Ce^{3+} to Ce^{4+} strongly influences charge trapping and recombination processes and has been reported in various Ce^{3+}-doped materials.[29–32]

In this work, we investigate the role of Ce^{3+} incorporation in the $Ca_3MgSi_2O_8$ lattice and its influence on the photochromic, TSL, and OSL properties of this host. This study provides a comprehensive analysis of dopant-induced point defects, their role in spectroscopic properties, and reports a novel multimodal photochromic material with improved spectroscopic properties for storage and dosimetry applications.

2. Materials and methods

Polycrystalline ceramic samples with nominal composition of $Ca_{3(1-x)}Ce_{3x}MgSi_2O_8$ (x = 0–0.005) were synthesized using a high-temperature solid-state synthesis method. High-purity MgO (99.99%, Fisher Scientific), $CaCO_3$ (99.999%, Merck), SiO_2 (99.999%, Fisher Scientific), $Ce(NO_3)_3{\cdot}6H_2O$ (99.999%, Carl ROTH), and H_3BO_3 (99.999%, Carl ROTH) were used as starting materials. To reduce the synthesis temperature and prevent the decomposition of $Ca_3MgSi_2O_8$, 5 mol% H_3BO_3 was introduced by partially substituting the corresponding amount of SiO_2. Stoichiometric amounts of the precursors were mixed and homogenized by grinding in an agate mortar using acetone as a wet-milling medium. To ensure precise Ce^{3+} control in samples with low dopant concentration (0.005–0.01%), an appropriate amount of $Ce(NO_3)_3{\cdot}6H_2O$ was dissolved in deionized water to prepare a 0.001 mol L^{-1} solution, which was added to the other precursors. For samples doped with 0.05–0.5% Ce^{3+}, the precursor was added without additional preparation. After mixing and drying, the precursor mixtures were pressed into 13 mm pellets using a uniaxial press from Specac Ltd. The pellets were placed on graphite plates and sintered in a tube furnace (HTRH 18/100/600, Carbolite Gero) at 1350 °C for 10 h under a reducing H_2/Ar atmosphere (5%/95%), with a heating and cooling rate of 5 °C min^{-1}. The resulting samples are denoted as CMS y%, where y represents the Ce^{3+} concentration relative to Ca^{2+} ions, expressed as mol%.

The phase composition of the prepared samples was analyzed by X-ray diffraction (XRD) using a Rigaku MiniFlex 600 powder diffractometer (Cu Kα radiation, operated at 40 kV and 15 mA) with Bragg–Brentano θ–2θ geometry.

PL and photoluminescence excitation (PLE) spectra were measured using the Edinburgh Instruments FLS1000 spectrometer with a 450 W Xenon arc lamp Xe2 from Edinburgh Instruments as the excitation source.

X-ray absorption spectra of CMS 0.1% and 0.5% were collected at the Ce L_3-edge (5723 eV) at room temperature using fluorescence detection at the P64 Advanced X-ray Absorption Spectroscopy beamline of DESY PETRA III.[33] The storage ring was operated at 6 GeV with a beam current of 120 mA in a multi-bunch mode. A fixed-exit, liquid-nitrogen-cooled Si(111) double-crystal monochromator was employed to select the incident photon energy from the undulator source, while higher harmonics were suppressed using two silicon mirrors. The incident X-ray intensity was monitored with a nitrogen-filled ionization chamber, and the fluorescence signal was detected using a passivated implanted planar silicon (PIPS) detector. Both the incidence angle of the X-ray beam relative to the sample and the detection angle relative to the detector were set to 45 degrees. Two reference compounds (CeO_2 99.99%, Alfa Aesar, and CeF_3 99.9%, Alfa Aesar) were used for comparison. The samples were prepared as pressed pellets.

The Ce L_3-edge X-ray absorption near-edge structure (XANES) and extended X-ray absorption fine structure (EXAFS) signals were extracted using the XAESA software,[34] following a standard data-processing procedure.[35] The experimental EXAFS spectra $\chi(k)$, where k denotes the photoelectron wavenumber, were qualitatively analyzed by comparison with theoretical spectra calculated within the multiple-scattering (MS) framework using the FEFF8.50L code.[36] Inelastic photoelectron losses were taken into account using the complex Hedin–Lundqvist exchange–correlation potential.[37] The MS calculations were carried out for atomic clusters with a radius of 8 Å, centered on the absorbing cerium atom and generated from the ideal crystallographic structures of monoclinic $Ca_3MgSi_2O_8$ (space group $P2_1/a$, No. 14).[38] No structural relaxation was included, and thermal disorder effects were neglected. Three structural models were examined, corresponding to cerium atoms occupying three distinct, non-equivalent crystallographic sites originally occupied by calcium atoms.[38]

Diffuse reflectance spectra were recorded using a double-beam spectrophotometer (Specord 210). Photochromic excitation and bleaching experiments were performed using a wavelength-tunable pulsed solid-state laser (Ekspla NT342/3UV). For photochromic excitation measurements, the laser power was adjusted to 0.7 ± 0.1 mJ, and the samples were irradiated at a selected excitation wavelength for 1 min, after which the diffuse reflectance spectrum was recorded. Following each measurement, the photochromic effect was bleached by irradiating the sample at 450 nm for 1 min. For photochromic bleaching measurements, the samples were first excited at 250 nm (1.2 ± 0.2 mJ) for 1 min to induce photochromism. Subsequently, bleaching was performed by irradiating the sample at a selected wavelength for 1 min, after which the diffuse reflectance spectrum was recorded. After each bleaching measurement, the samples were additionally irradiated at 450 nm for 1 min to remove any residual photochromic signal.

OSL spectra were measured using a wavelength-tunable laser Ekspla NT342/3UV as an irradiation and optical stimulation source. Prior to the measurements, the samples were irradiated with 250 nm for 1 min. For the OSL decay measurements, a stimulation wavelength of 450 nm was selected to ensure maximum stimulation efficiency. OSL emission spectra were recorded using 480 nm excitation to minimize spectral

overlap between the stimulation light and the Ce^{3+} emission band. The signal was detected using an Andor iSTAR DH734 CCD camera coupled to an Andor SR-303i-B spectrometer.

TSL glow curves were obtained using the Lexsyg research Fully Automated TL/OSL Reader from Freiberg Instruments GmbH. Irradiation was performed with an X-ray tube (40 kV, 0.5 mA, W-anode) and a Q-switched UV laser DTL-389QT (263 nm) from the Laser-compact Group. The TSL curves were recorded with a Hamamatsu R13456 photomultiplier tube and an Andor SR-303i-B spectrometer paired with a DV420A-BU2 CCD camera. The system was operated at a constant heating rate of 1 °C s^{-1}. For dose dependence measurements, a Risø TL/OSL reader (model DA-22) was used. The reader is equipped with a $^{90}Sr/^{90}Y$ beta source with a maximum energy of 2.27 MeV and an activity of 1.48 GBq. Irradiation of the analyzed samples was carried out using this beta source at a dose rate of 0.1237 Gy s^{-1}, which was determined using a quartz reference calibrated with a ^{60}Co gamma source. The reproducibility of the TSL signal was determined for four different irradiation doses in the low dose range of 0.2–0.6 Gy by repeating the measurement four times. The coefficient of variation was calculated for the integral TSL signal intensity.

The Bruker ELEXSYS-II E500 CW-EPR spectrometer was used to investigate the samples by electron paramagnetic resonance (EPR). All EPR spectra were acquired at room temperature. X-band measurements (9.83 GHz) were performed at a microwave power of 0.10 mW, while for Q-band measurements (34.00 GHz), the power was optimized to 0.01 mW. For comparison, EPR signal intensities are normalized to 100 mg of sample. Either wavelength-tunable laser Ekspla NT342/3UV or an X-ray lamp operated with 45 kV and 10 mA was used for sample irradiation. Stepwise sample annealing after the irradiation was performed in a custom-built furnace, with each annealing step maintained for 5 minutes. EPR spectra simulations were performed using the MATLAB-based open-source toolbox – EasySpin.[39]

3. Results and discussion

The crystal structure of $Ca_3MgSi_2O_8$ is shown in Fig. 1a. It has monoclinic symmetry ($P2_1/a$) with 4 formula units per unit cell and consists of SiO_4 tetrahedra, MgO_6 octahedra, and three non-equivalent Ca atoms in nine-fold (Ca1), eight-fold (Ca2), and ten-fold (Ca3) coordination. All of the prepared samples have single-phase monoclinic $Ca_3MgSi_2O_8$, which is confirmed by powder XRD analysis shown in Fig. 1b. All diffraction peaks can be indexed to the reference pattern of $Ca_3MgSi_2O_8$ (PDF 01-086-3096), and no additional reflections related to secondary or impurity phases are observed. The increase in Ce^{3+} content does not promote the formation of other crystalline compounds, suggesting that the Ce^{3+} ions are incorporated in the $Ca_3MgSi_2O_8$ lattice. However, due to low dopant concentration, it does not induce a detectable shift in XRD peak position. Due to the similarity in ionic radii of Ca^{2+} and Ce^{3+} (1.12 Å and 1.143 Å for eight-fold coordination, respectively),[40] Ce^{3+} can be expected to incorporate in Ca^{2+} positions.

The PLE spectra shown in Fig. 1c exhibit two dominant bands with maxima at 270 and 310 nm, which are assigned to the allowed 4f → 5d transitions of Ce^{3+}. Upon excitation with 270 nm, a broad emission band centered at ~370 nm is observed; it is attributed to 5d → 4f transitions of Ce^{3+}. Similar emission signals have been detected in other Ce^{3+} doped oxides.[41–43] With increasing Ce^{3+} concentration, the emission maximum shifts slightly from 368 to 377 nm. This shift may originate from the reabsorption of Ce^{3+} emission due to the overlap of emission and excitation spectra. Some contribution could also be associated with the incorporation of Ce^{3+} ions into multiple crystallographic sites or with lattice distortion induced by the substitution of larger Ce^{3+} ions on Ca^{2+} sites. Such structural modifications are expected to alter the local crystal field strength and covalency, leading to a centroid shift of the Ce^{3+} 5d levels and a corresponding shift of the emission band to longer wavelengths.[44] Previous PL studies of Ce^{3+}-doped $Ca_3MgSi_2O_8$ have detected two distinct Ce^{3+} centers, which were associated with the incorporation of Ce^{3+} ions in two Ca^{2+} sites in the host lattice.[43] To clarify the Ce^{3+} substitution, X-ray absorption spectroscopy measurements were performed.

The Ce L_3-edge XANES spectra of the CMS 0.5% and two reference compounds (CeO_2 and CeF_3) are compared in Fig. 2a. The XANES spectra of reference compounds agree well with the previously reported spectra.[45,46] The spectrum of CeF_3 is

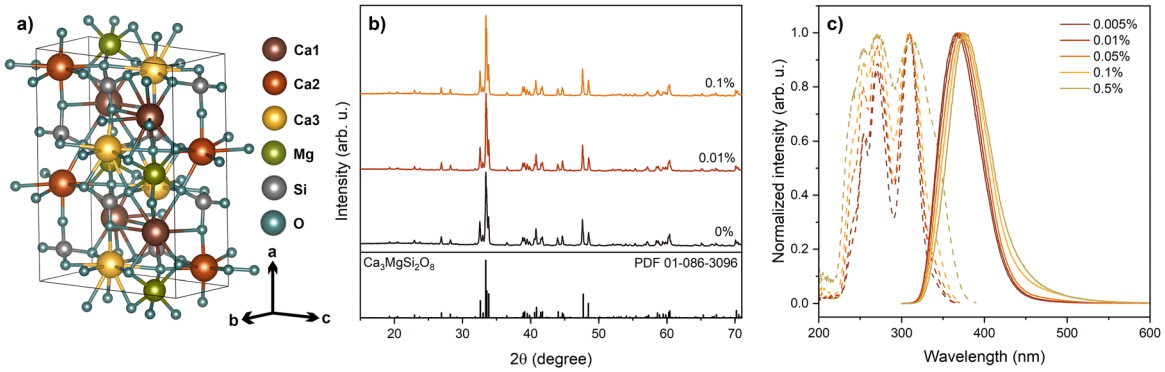

Fig. 1 (a) Crystal structure of $Ca_3MgSi_2O_8$; (b) XRD patterns of CMS 0–0.1%; (c) PLE spectra for the 370 nm emission and PL spectra excited with 270 nm of CMS 0.005–0.5%.

dominated by a prominent absorption peak, the so-called "white line", located at about 5726 eV and attributed to $2p_{3/2}$ → 5d dipole-allowed transition with the final excited state $4f^15d^1$ of Ce^{3+}. In contrast, the XANES spectrum of CeO_2 has a small pre-edge peak at about 5720 eV, followed by the shoulder at *ca.* 5727 eV, and two main peaks at approximately 5731 and 5738 eV. A detailed discussion of the CeO_2 XANES based on a high-energy resolution fluorescence mode (HERFD) experiment and theoretical simulations, including previous studies, was recently published by Kvashnina.[47] The pre-edge peak was attributed to the quadrupole-allowed $2p_{3/2}$ → 4f transitions at the bottom of the CeO_2 conduction band. The two main peaks are, respectively, due to the final states, reflecting the mixing of $4f^1L$ (L denotes a hole in the O 2p band) and $4f^0$ configurations in the ground state. Note that the crystal-field splitting of the Ce 5d band leads to further broadening of the main peaks and is responsible for the shoulder.[48] The XANES spectrum of the CMS 0.5% sample is dominated by a strong "white line", and its edge position is closer to that of CeF_3. The comparison between the first derivatives of the absorption coefficients of CMS samples doped with 0.1% and 0.5% Ce^{3+} and those of the reference compounds CeO_2 and CeF_3 is shown in Fig. 2b. The position of the absorption edge, determined by the maximum of the first derivative, for CMS 0.1% coincides with that for CMS 0.5% and is close to that for CeF_3. This supports the presence of cerium ions predominantly in the 3+ oxidation state in the CMS structure.

To understand the location of Ce^{3+} ions in the CMS structure, the calculated EXAFS spectra of cerium atoms located at three different Ca^{2+} crystallographic sites in monoclinic $Ca_3MgSi_2O_8$[38] are compared with the experimental data for $Ca_3MgSi_2O_8$:0.5% Ce^{3+} (Fig. 2c and d). Due to the limited quality of the experimental data, only a qualitative comparison of the EXAFS spectra can be performed over a restricted energy range up to k = 6.5 $Å^{-1}$. Among the three sites, the EXAFS spectrum of cerium substituting for Ca2 agrees best with the experimental data in both k and R space. In contrast, the EXAFS spectrum of Ce at the Ca1 site fails to reproduce the beating observed around k = 5 $Å^{-1}$. Moreover, the EXAFS spectra of Ce at both the Ca1 and Ca3 sites are unable to reproduce the shape of the double peak in the Fourier transform.

Next, we compare the local environments of the three Ca sites in terms of coordination number, average interatomic distance, and shell distortion. At the Ca1 site, calcium is surrounded by nine oxygen atoms, with an average Ca–O distance of 2.73 Å and a standard deviation of σ = 0.18 Å. At the Ca2 site, calcium exhibits eightfold coordination, with the smaller average Ca–O distance of 2.62 Å, and the shell distortion is the largest (σ = 0.20 Å) due to the presence of a single short Ca–O bond of 2.18 Å. At the Ca3 site, calcium is surrounded by ten oxygen atoms, with an average Ca–O distance of 2.64 Å and a standard deviation of σ = 0.15 Å. Thus, the proposed preference of cerium ions for the Ca2 site suggests

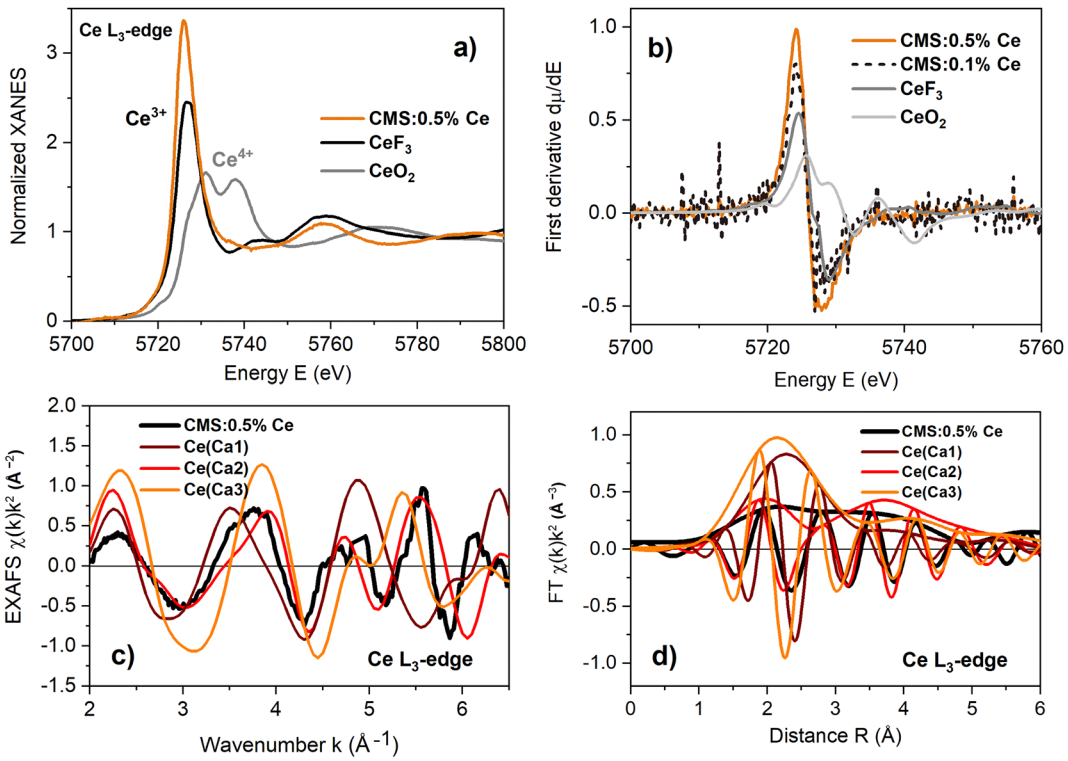

Fig. 2 (a) The Ce L_3-edge XANES spectra of CMS 0.5% and the reference compounds CeO_2 and CeF_3. (b) Comparison of the first derivatives dμ/dE of the absorption coefficients of CMS 0.1% and 0.5% and the reference compounds CeO_2 and CeF_3. Comparison of the experimental (black curves) Ce L_3-edge (c) EXAFS spectra $\chi(k)k^2$ and (d) their Fourier transforms (FTs) with three calculated EXAFS spectra, corresponding to cerium atoms placed at Ca1 (brown curves), Ca2 (red curves), and Ca3 (orange curves) crystallographic sites in monoclinic $Ca_3MgSi_2O_8$.[38]

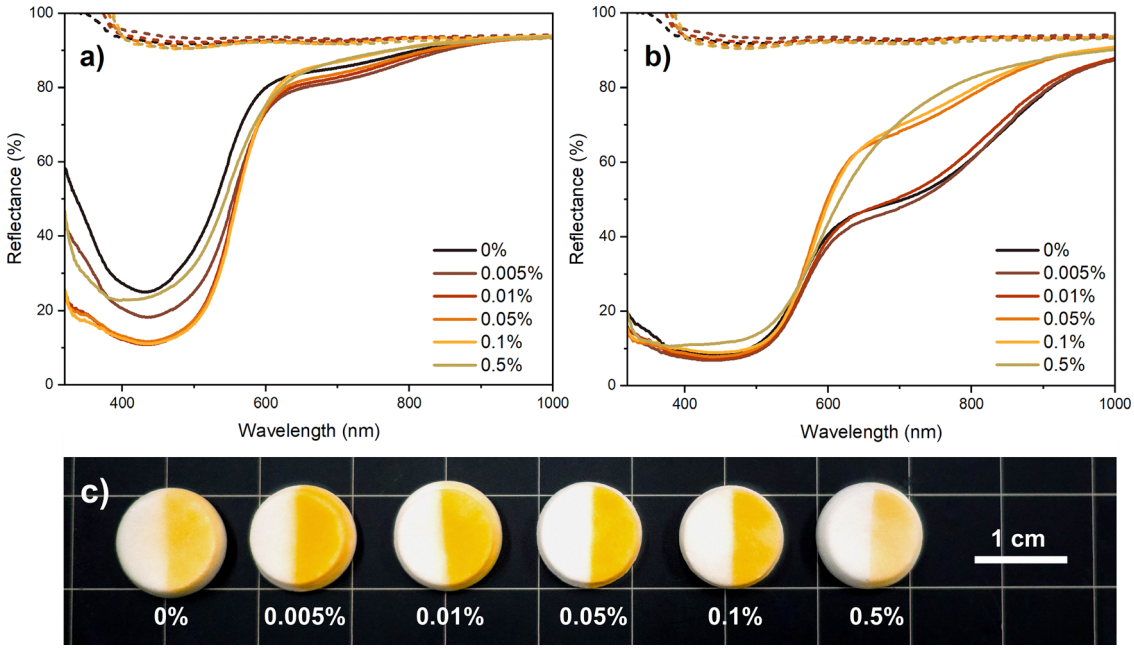

Fig. 3 Diffuse reflectance spectra of CMS 0–0.5% before irradiation (dashed lines), after (a) 250 nm and (b) X-ray irradiation (solid lines); (c) photograph of CMS samples after irradiation of the right side with 250 nm.

that cerium mainly adopts a distorted eightfold coordination to oxygen.

All samples, including undoped $Ca_3MgSi_2O_8$, exhibited a photochromic effect. The diffuse reflectance spectra of CMS samples before and after irradiation with 250 nm are shown in Fig. 3a. No significant absorbance, except for a decrease in reflectance in the UV range due to Ce^{3+} 4f → 5d excitation (see Fig. 3b), is observed before irradiation. After UV irradiation, all samples display a strong photoinduced absorption, characterized by a dominant band in the blue spectral region with a maximum at 430 nm and a weaker shoulder extending into the red-NIR region. This strong absorption results in the vibrant yellow coloration shown in Fig. 3c. The presence of multiple absorption bands suggests the formation of more than one type of photochromic color center within the $Ca_3MgSi_2O_8$ host lattice.

The photochromic efficiency for the blue absorbance band was calculated as the normalized intensity difference between the irradiated and unirradiated state:

$$\Delta R_{\text{norm}} = \frac{R_0 - R_1}{R_0} \times 100 \quad (1)$$

where R_0 and R_1 are reflectance at 430 nm before and after irradiation, respectively. The photochromic efficiency increases from 72% in the undoped sample to 87–88% for CMS 0.01–0.1%, before decreasing to 74% in the sample with the highest Ce^{3+} concentration (CMS 0.5%). The exceptionally high photochromic efficiency observed for this system, compared with other reported photochromic hosts,[1] indicates the strong potential of $Ca_3MgSi_2O_8$ for practical applications. The variation in photochromic efficiency with Ce^{3+} concentration suggests that Ce^{3+} ions improve the recombination processes in $Ca_3MgSi_2O_8$, likely by participating in charge trapping during excitation. It can be expected that Ce^{3+} acts as a hole trap, similar to Eu^{2+} in $Ca_3MgSi_2O_8$, as reported previously.[28]

The color change in CMS samples can also be induced by irradiation of other high-energy sources. The diffuse reflectance spectra before and after irradiation with X-rays are shown in Fig. 3b. The spectra consist of the same absorption bands as observed after UV excitation; however, their intensity and relative ratio have changed. The overall intensity of the absorbance is higher after X-ray irradiation in comparison to UV. The radiochromic efficiency of the dominant band, calculated using eqn (1), ranges from 89% to 93%. The intensity of the dominant band does not significantly change with the increase of Ce^{3+} content, suggesting that the defects responsible for this band are intrinsic to the $Ca_3MgSi_2O_8$ host lattice. However, the intensity of the red-NIR absorption band is considerably stronger after X-ray irradiation, indicating that the defects related to this band are more efficiently generated by high-energy radiation. A gradual decrease in the intensity of this band with increasing Ce^{3+} content suggests that Ce^{3+} incorporation suppresses the formation or stabilization of these defects.

The diffuse reflectance analysis suggests that Ce^{3+} primarily improves the efficiency of UV-induced photochromism by affecting the charge trapping processes during photochromic excitation. It does not significantly affect the formation of charge traps associated with the dominant absorbance band in the blue spectral range; however, it does alter the formation of defects associated with the weaker absorbance band in the red-NIR range.

The photochromic effect in the CMS is reversible and can be bleached both with visible light and heat. The diffuse reflectance spectra before irradiation, after irradiation, and after

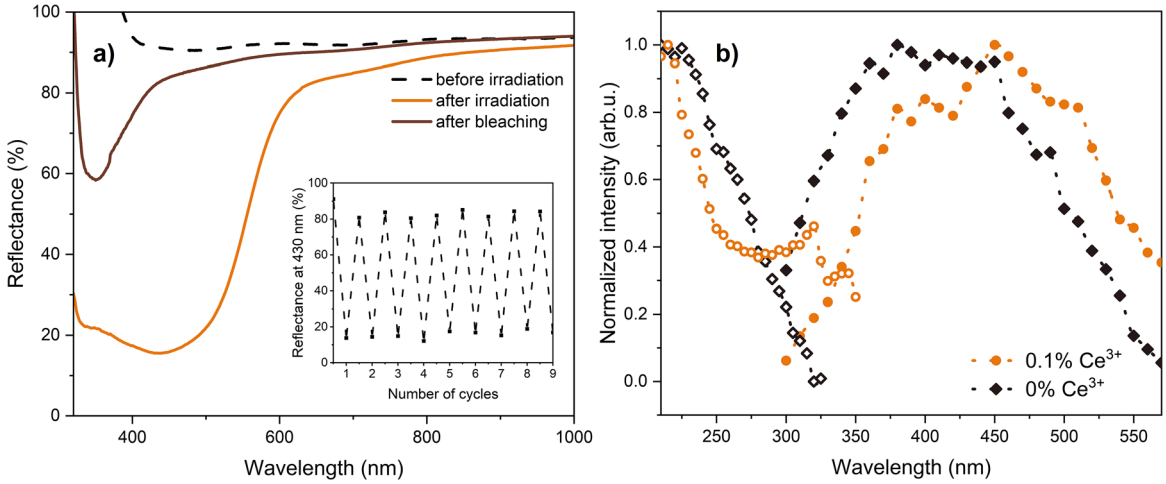

Fig. 4 (a) Diffuse reflectance spectra of CMS 0.1% before irradiation, after irradiation with 250 nm, and after bleaching with 450 nm. Inset: changes in reflectance at 430 nm after multiple irradiation and bleaching cycles. (b) Photochromic excitation (empty symbols) and photochromic bleaching (solid symbols) spectra of undoped CMS and doped with 0.1% Ce^{3+}.

optical bleaching are shown in Fig. 4a. The reflectance spectra after bleaching are similar to those before irradiation, indicating that most of the defects can be efficiently stimulated with 450 nm; however, there is a slight residual signal around the 345 nm range. The presence of this signal suggests that the wide absorption band in the blue spectral range likely consists of multiple bands related to defects with different stimulation efficiencies. No significant changes in reflectance can be detected after multiple irradiation and bleaching cycles, indicating that color centers can be created repeatably and there is no degradation of photochromic properties.

To analyze the role of Ce^{3+} ions in the photochromic properties of $Ca_3MgSi_2O_8$, photochromic excitation and photochromic bleaching or stimulation spectra were measured for undoped CMS and CMS 0.1%. The results are shown in Fig. 4b. The maximum photochromic excitation efficiency for both samples is in the deep UV range around 210–230 nm. The undoped sample shows a continuous decay in intensity from 210 to 325 nm. In contrast, the sample doped with 0.1% Ce^{3+} shows a minimum at approximately 270 nm, beyond which the intensity increases. This spectral range corresponds to the excitation of 4f → 5d transitions of Ce^{3+} (Fig. 1c). The photochromic bleaching or stimulation spectra of both samples consist of a broad band with a maximum in the 380–470 nm range. The band of CMS 0.1% is shifted to longer wavelengths, possibly due to increased photochromic excitation efficiency in the near-UV range in comparison to the undoped sample. The photochromic excitation and stimulation data indicate that the introduction of Ce^{3+} into $Ca_3MgSi_2O_8$ affects photochromic excitation efficiency, especially in the near-UV range, which corresponds to the optical absorption of Ce^{3+}. These results suggest that Ce^{3+} ions participate in the photochromic process by acting as charge traps. The electron can be liberated from the 5d excited state, resulting in the photoionization of Ce^{3+} to Ce^{4+}.

In addition to the photochromic effect, both OSL and TSL signals can be detected in CMS samples. OSL signals were observed in all samples except for undoped CMS (Fig. 5a). The OSL emission spectra are similar to the PL spectra shown in Fig. 1c and are dominated by the characteristic 5d → 4f transitions of Ce^{3+}. The photochromic excitation data shown in Fig. 4b indicate that Ce^{3+} is photoionized during the UV excitation; therefore, it can be expected to act as a recombination center during optical stimulation. A slight spectral shift of the OSL emission relative to PL is observed in the sample with the highest Ce^{3+} content, which might be attributed to the selective participation of specific Ce^{3+} centers during the OSL process.

The OSL decay is shown in Fig. 5b. It becomes faster with increasing Ce^{3+} concentration. This behavior suggests improved recombination efficiency, which can be due to an increased density of recombination centers and a smaller distance between trapped charge carriers and Ce^{3+} ions. In addition, higher dopant concentration can facilitate tunneling-assisted recombination, resulting in faster charge release and decay kinetics. It should be noted that the fastest OSL decay was detected in CMS 0.1%, and it was slightly slower in the sample with the highest Ce^{3+} content (CMS 0.5%), which could be due to a lower overall concentration of charge traps, indicated by the lower TSL and EPR signal intensities of this sample, analyzed further.

For additional analysis of the charge trap properties, TSL glow curves were measured after irradiation with X-rays and UV. TSL glow curves after X-ray irradiation are shown in Fig. 6a, and after UV irradiation are provided in Fig. S1. The general structure of glow curves for both X-ray and UV irradiation is similar, consisting of four main glow peaks with maxima (T_{max}) around 80, 130, 230, and 360 °C, regardless of the excitation source, indicating that the same charge traps and trapping and detrapping mechanisms are involved. Conversely, there is a notable difference in intensity between samples irradiated with UV and those with X-rays, with the latter showing considerably higher intensity. This is consistent with diffuse reflection spectra measurements shown in Fig. 3a and b. In all samples

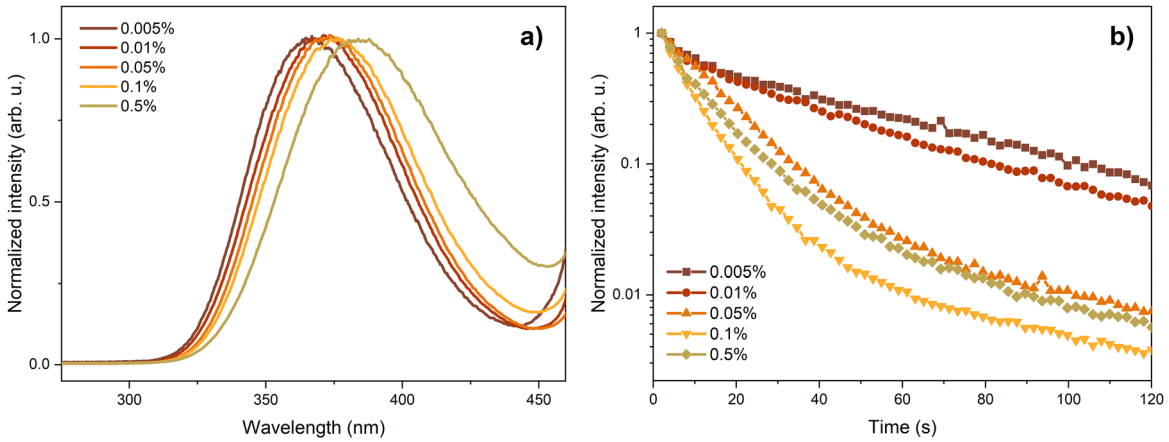

Fig. 5 (a) OSL spectra stimulated with 480 nm and (b) OSL decay detected during stimulation with 450 nm of CMS samples doped with 0.005–0.5% Ce^{3+}.

except the CMS 0.5%, the TSL maximum intensity is reached around 230 °C; moreover, in samples with low Ce^{3+} concentration and the undoped sample, weaker glow peaks are either not detectable or absent. The TSL glow curve of the CMS 0.5% deviates from the rest of the set; the same was observed in the OSL measurements.

The TSL emission signals shown in Fig. 6b consist of two dominant signals – a peak at around 370 nm corresponding to 5d → 4f transitions of the Ce^{3+} ion and a broad red luminescence band with a maximum around 690 nm. In the undoped sample, this red emission band is the dominant TSL signal. This emission signal is detectable in the PL spectra; however, due to the overlap of the PLE spectrum with the defect stimulation in UV, it cannot be detected without simultaneous irradiation of the material. The excitation and emission spectra for the red emission band in CMS 0% are provided in Fig. S2. This indicates that the band is likely associated with radiation-induced intrinsic defect recombination. The relative intensity of the red emission band gradually decreases with Ce^{3+} concentration, likely due to an increase in competing recombination or emission centers.

To analyze the activation energies E_a of the charge traps and their nature, the X-ray-irradiated CMS 0.1% sample was chosen due to the highest overall intensity. For analysis, the well-established T_{max}–T_{stop} measurement technique, together with Initial Rise Analysis (IRA), was applied. Both methods are widely acknowledged and used in advanced trap analysis.[49–52] The resulting glow curves from the T_{max}–T_{stop} experiment are

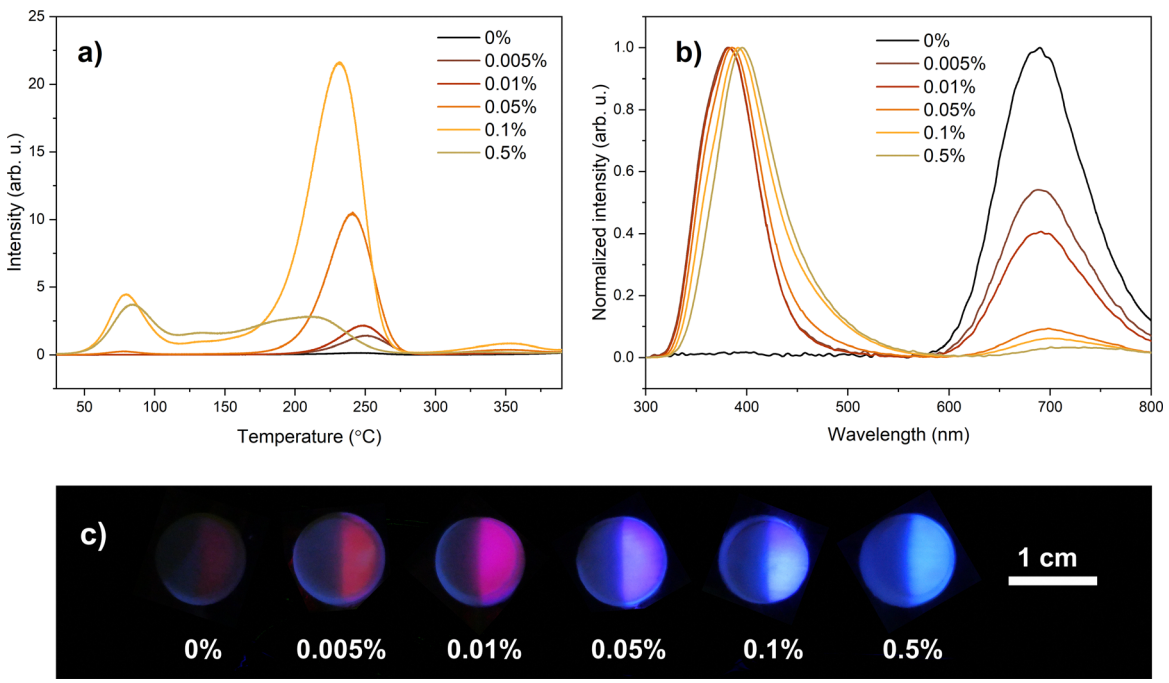

Fig. 6 (a) TSL glow curves and (b) TSL emission spectra of CMS samples detected at 230 °C after irradiation with X-rays for 8 s; (c) photographs of CMS samples with the right side irradiated with 250 nm detected during heating at ~230 °C.

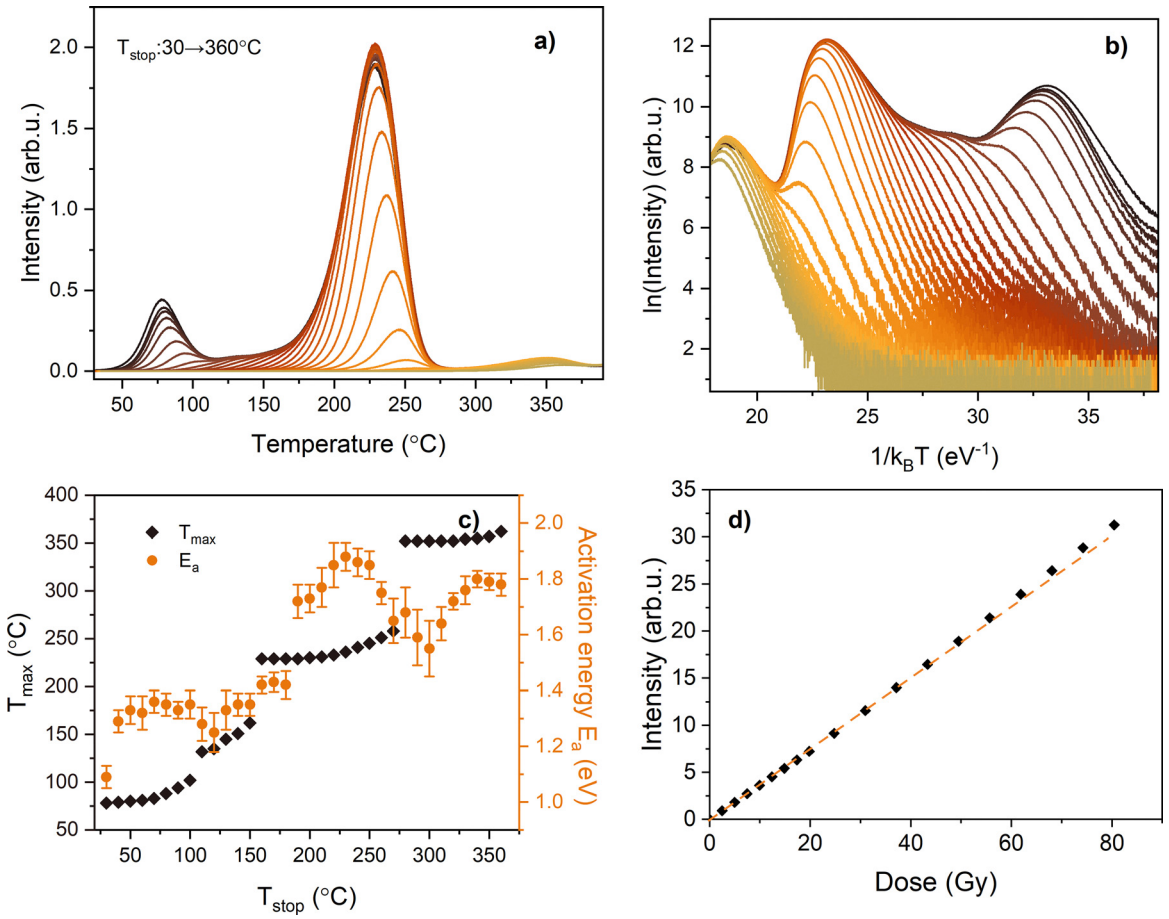

Fig. 7 (a) TSL glow curves of the CMS 0.1% sample after preheating up to different T_{stop} values between 30 and 360 °C with a 10 °C step. The samples were irradiated with X-rays for 8 s before each preheating; (b) IRA plots of the glow curves obtained from the T_{max}–T_{stop} experiments; (c) corresponding T_{max}–T_{stop}/E_a–T_{stop} plots; (d) TSL intensity dependence on beta irradiation dose of CMS 0.1%.

shown in Fig. 7a. The temperature step for T_{stop} was 10 °C from 30 to 360 °C. The corresponding IRA plots are depicted in Fig. 7b, and T_{max}–T_{stop} and E_a–T_{stop} plots are shown in Fig. 7c. From the T_{max}–T_{stop} TSL glow curve, four regions can be roughly distinguished, with three clear peaks corresponding to traps with activation energies of 1.30 ± 0.07 eV (T_{max} ≈ 80 °C); 1.79 ± 0.12 eV (T_{max} ≈ 230 °C); and 1.70 ± 0.09 eV (T_{max} ≈ 360 °C). The fourth region, near 130 °C, is characterized not by a distinct glow peak but by an intensity plateau. In this region, T_{max} and E_a grow as T_{stop} increases; E_a rises from approximately 1.30 eV to 1.40 eV. Such TSL bands have been previously understood to be associated with thermally assisted tunneling processes.[53,54] Another non-typical behavior of the results is smaller E_a values corresponding to higher T_{max}, as seen in the 1.79 ± 0.12 eV (T_{max} ≈ 230 °C) and 1.70 ± 0.09 eV (T_{max} ≈ 360 °C) glow peaks. It is reasonable to link this behavior to thermally assisted tunneling as well. In this case, the E_a value would represent the energy difference between the ground level and the tunneling level of the trap, rather than the energy required to overcome the gap between the trap and the conduction band as in the classical TSL process.[55,56] Although similar results have been reported in earlier studies, a clear explanation has not yet been established, and drawing definitive conclusions would require further research beyond the scope of this study.[57–59]

CMS 0.1% was selected for dose-dependence measurements using beta particles. Fig. 7d shows the dependence of the TSL signal intensity on the absorbed dose. A linear response was observed up to approximately 40 Gy (R^2 = 0.9997). Beyond this threshold, the intensity demonstrates a supralinear dose response – a phenomenon observed in multiple TSL dosimetry materials.[60,61] At low doses, the response is primarily governed by the population of isolated trapping centers, resulting in a linear dose dependence. At higher irradiation doses, processes such as saturation of competitive non-radiative charge traps and an increase in delocalized recombination processes can lead to supralinear response.[60] The TSL signal showed good reproducibility, and the coefficient of variation for TSL intensity, analyzed for selected points in the 0.2–0.6 Gy range, ranged from 1.9 to 3.6%. The results indicate that CMS has potential as a TSL dosimetry material. However, further research is required to analyze the fading rate, response to different excitation sources, and precisely determine the minimal irradiation dose.

To analyze the key point defects related to the spectroscopic properties of CMS, EPR spectroscopy was used. EPR spectra of

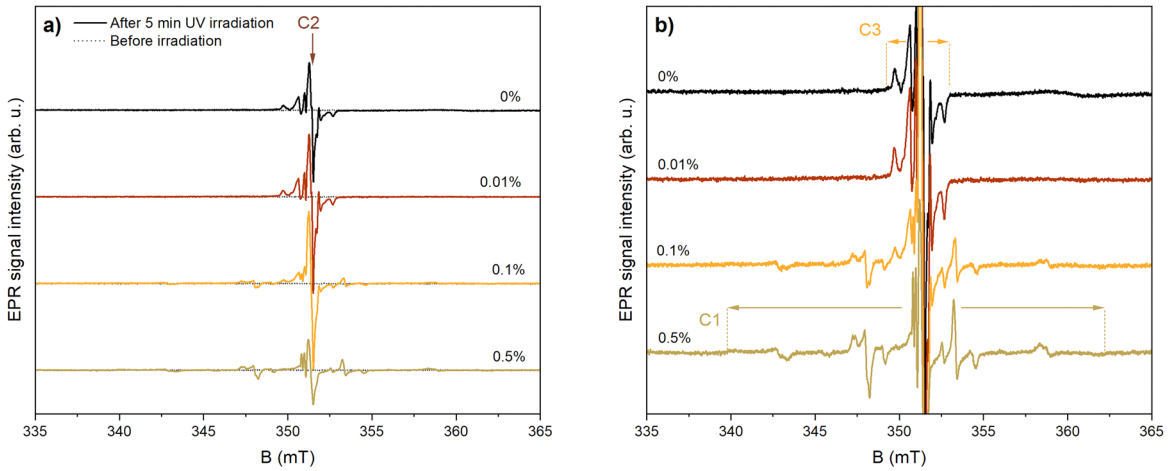

Fig. 8 X-band EPR spectra of the investigated samples before and after 250 nm irradiation: (a) full intensity and (b) magnified scale.

the investigated CMS samples with different concentrations of Ce before and after UV irradiation are shown in Fig. 8. No signals were detected before the irradiation. After irradiation using X-rays or UV, a strong EPR signal appears. The EPR spectra detected after irradiation with different sources were similar (Fig. S3).

Based on the stability of the UV-generated signals (Fig. 10), three components (C1, C2, and C3) can be differentiated in the EPR spectra. Components C2 and C3 were previously reported in Eu^{2+}-doped $Ca_3MgSi_2O_8$.[27] Component C2 is a slightly anisotropic signal at *ca.* 351 mT (g_1 = 2.0007, g_2 = 1.9997, g_3 = 1.9990) with the highest peak-to-peak intensity. The overlapping C3 contribution has similar g-factor values (g_1 = 2.0006, g_2 = 2.0000, g_3 = 1.9994), but a more complex signal profile due to anisotropic hyperfine (HF) interaction with a single boron nucleus (A_1^{11B} = 11 MHz, A_2^{11B} = 28 MHz, A_3^{11B} = 10 MHz). Both signals have been assigned to F^+-type centers (singly occupied oxygen vacancies), where boron impurities play a stabilizing role on the second paramagnetic center.[27] This is consistent with the differences in annealing curves presented in Fig. 10c. The EPR spectra of both centers show a decrease in intensity at the highest Ce^{3+} concentration (Fig. 8), which suggests that the dopant ion introduces competing trapping pathways in the material. This hypothesis is supported in Fig. 8b, where a broad signal in the 340–360 mT range, denoted as C1, increases with cerium concentration.

Simulations of EPR spectra acquired at two microwave frequencies (X- and Q-band) were carried out to determine the spin-Hamiltonian (SH) parameters of signal C1 using the following equation:

$$\hat{H} = \mu_B \vec{B} g \hat{S} + \hat{S} A \hat{I} \quad (2)$$

In eqn (2), g is the g-factor; μ_B – the Bohr magneton; $\vec{B}$ – external magnetic field; $\hat{S}$ – electronic spin operator; A – HF coupling tensor with ^{10}B (I = 3; natural abundance = 19.9%) and ^{11}B (I = 3/2; 80.1%) nuclei; $\hat{I}$ – nuclear spin operator.[62] The best fit, shown in Fig. 9, was achieved using S = 1/2 with the following set of SH parameters: g_1 = 2.0015(1), g_2 = 2.0016(1), g_3 = 2.0006(1); and ^{11}B HF couplings A_1^{11B} = 139(1) MHz

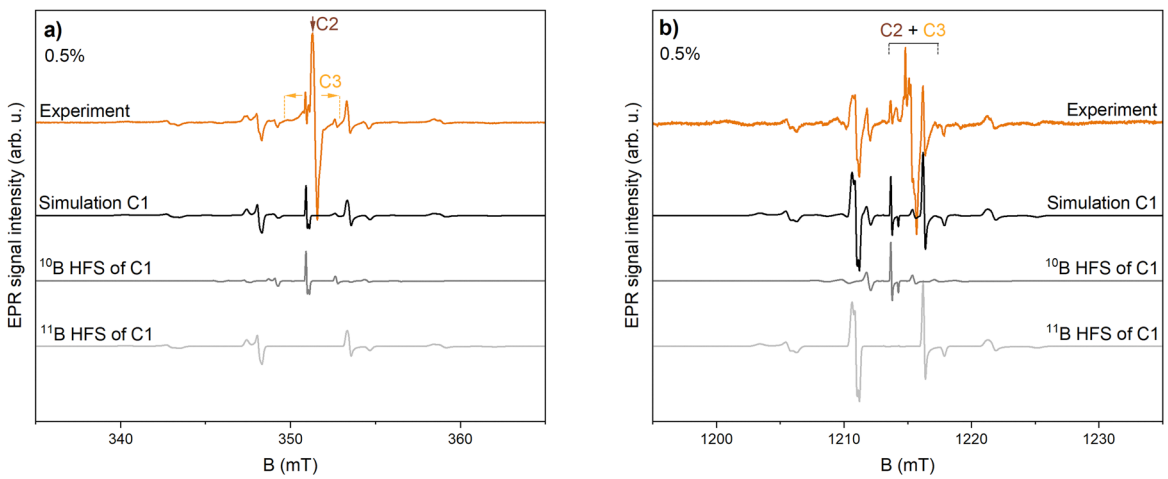

Fig. 9 Simulations of the C1 EPR component acquired at (a) X-band and (b) Q-band microwave frequencies.

A_2^{11B} = 150(1) MHz, A_3^{11B} = 204(2) MHz. The experimental HF structure is well reproduced by a superposition of simulated contributions from ^{10}B and ^{11}B weighted by their natural abundances and using the respective nuclear magnetic moments, thereby supporting the selected spin system.

Comparison of the EPR simulation results with the literature data allows us to propose a boron-associated electron center model for the C1 component in cerium-doped CMS. EPR studies of radiation-induced paramagnetic centers in LiB_3O_5, $Li_2B_4O_7$, and BaB_2O_4 crystals report electron-type centers attributed to trapped electrons at oxygen vacancies forming adjacent to boron atoms.[63–66] In $Li_2B_4O_7$, the trapped electron is localized primarily on one of the two boron ions adjacent to the oxygen vacancy, leading to pronounced ^{11}B HF couplings.[65] In BaB_2O_4, the trapped electron shows ^{11}B HF splittings of 4.2–4.9 mT, corresponding to 120–140 MHz, and a g value of 1.9993, *i.e.*, slightly below the free electron g_e = 2.0023 value.[64] The negative shift of the principal components of the *g*-tensor relative to g_e and ^{11}B HF couplings in the hundreds of MHz range for C1 in CMS, allows us to propose a similar defect model of a trapped electron at an oxygen vacancy (F^+-type center) coupled strongly to a neighboring boron atom.

A plausible defect formation scenario in CMS is that boron introduced during synthesis (*via* borate-based additive) incorporates into the silicate lattice, forming a boron–oxygen unit. Local charge compensation processes can promote the formation of nearby oxygen vacancies, which act as charge traps. Following UV or X-ray irradiation, an electron can become trapped at such a vacancy in the vicinity of the boron impurity, giving rise to the C1 EPR signal. The observed increase in the C1 intensity with Ce concentration (Fig. 8b) suggests that Ce^{3+} substituting Ca^{2+} either stabilizes the relevant vacancy-boron complexes and/or serves as an electron donor for populating this trap. According to diffuse reflectance measurements of X-ray irradiated samples, the latter mechanism is the most probable.

Radiation-induced paramagnetic centers exhibit distinct stabilities during storage at room temperature and stepwise annealing (Fig. 10). At room temperature, C1 decays rapidly (to 0.54 of the initial intensity after 120 min), C2 is moderately stable (to 0.84 after 5 h), whereas C3 remains essentially

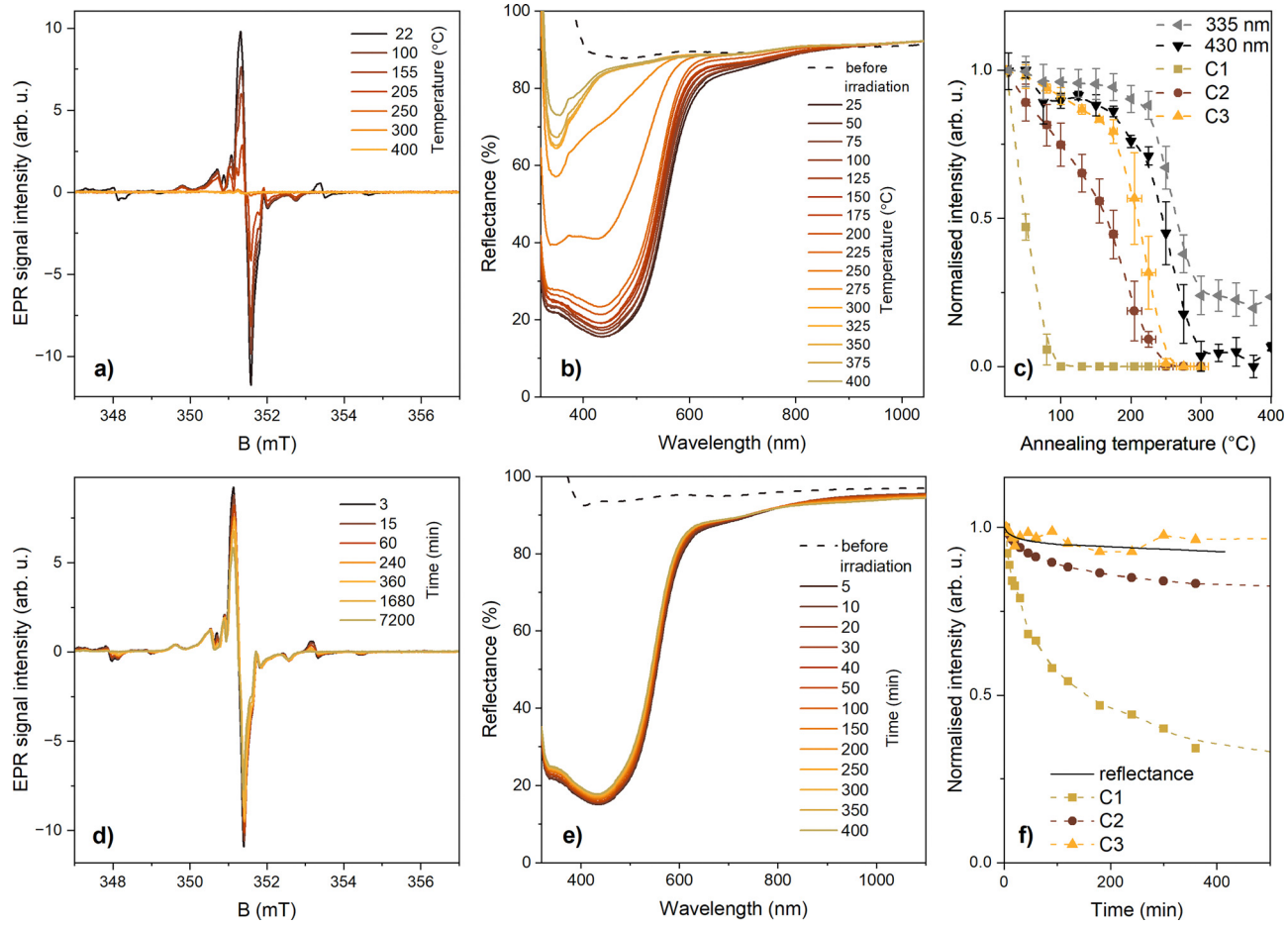

Fig. 10 (a) X-band EPR spectra, (b) diffuse reflectance spectra and (c) comparison of C1–C3 and dominant absorbance band (335 nm–430 nm) intensity of the CMS 0.1% after 250 nm irradiation and subsequent annealing; (d) X-band EPR spectra, (e) diffuse reflectance spectra and (f) comparison of C1–C3 and integral diffuse reflectance signal stability of the CMS: 0.1% after 250 nm irradiation and after storage of the sample in the dark for selected time intervals at room temperature.

stable within the experimental EPR signal intensity fluctuations. Similar trends of the C2 ("C unstable") and C3 ("C stable") components were reported in Eu^{2+}-doped $Ca_3MgSi_2O_8$.[27] The stepwise annealing data show that C1 is fully annealed by 100 °C, whereas C2 and C3 are more stable and anneal most rapidly in the 150–200 and 200–250 °C ranges, respectively. These annealing ranges are consistent with glow peak temperatures around 80, 130, and 230 °C in the TSL glow curves (Fig. 6 and 7), which indicates that these paramagnetic centers play a role in radiative recombination processes. Regardless of dissimilar thermal stabilities, all EPR signal components can be efficiently bleached by exposure to 430 nm light (Fig. S4). In diffuse reflectance spectra shown in Fig. 10b, the dominant signal corresponding to overlapping absorbance bands at 335 nm and 430 nm remains stable up to 200–250 °C. Slightly higher stability was detected for the 335 nm band, as expected from the lower optical bleaching efficiency shown in Fig. 4a. A similar thermal stability of the dominant absorbance band at 430 nm and C3 signal was detected (see Fig. 10c). The photochromic response of all the investigated materials exhibits excellent signal stability after storage in the dark. The changes in the integral signal intensity of CMS 0.1% are shown in Fig. 10e. The signal intensity after 400 min decreased only by 9%, and similar values were also detected in other samples including undoped CMS and CMS 0.5% shown in Fig. S5. The signal stability in CMS is exceptionally high in comparison to Eu^{2+}-doped $Sr_3MgSi_2O_8$ and $(Ca,Sr)_3MgSi_2O_8$ solid solutions reported previously,[27,28] indicating unusually high stability of the color centers in this host. The comparison of EPR and diffuse reflectance signals shown in Fig. 10f indicates a similar stability of C3 centers and the dominant absorbance band.

In summary, the introduction of Ce^{3+} does not promote the formation of color centers, but it improves the photochromic excitation efficiency, most likely due to photoionization of Ce^{3+} to Ce^{4+} during the excitation. The dominant paramagnetic point defects formed during the excitation are three distinct F^+ centers, two of which are located near the boron ions. The defects responsible for both the dominant absorbance band and the TSL signal in CMS are C3 centers. The trapped charges can be released thermally, resulting in TSL, or by optical stimulation, resulting in OSL.

The mechanism of defect-related optical properties of CMS is summarized in Fig. 11. In undoped CMS (Fig. 11a), the photochromic effect can be induced after UV irradiation, and the highest efficiency is in the deep UV range (210–230 nm). The electrons are likely excited from the valence to the conduction band and trapped at oxygen vacancies, thus forming F^+-type centers. Although three different F^+ centers can be detected in these materials, the dominant absorbance band and TSL signal can be attributed to the C3 center detected by EPR analysis. Electrons can be liberated from the trap centers by optical stimulation or heat. Optical stimulation in the undoped CMS results in the bleaching of the photochromic effect. The dominant TSL emission in the undoped samples is a broad band in the red spectral range, likely related to recombination of irradiation-induced centers. In CMS doped with Ce^{3+} (Fig. 11b), the photochromic effect can be induced by irradiation with deep UV (210–230 nm) or excitation of Ce^{3+} from 4f to 5d states, suggesting photoionization of Ce^{3+} to Ce^{4+}. Similar to the undoped sample, electrons can be trapped in the oxygen vacancies and subsequently liberated using optical stimulation or heating. Both OSL and TSL signals can be detected in all Ce^{3+} doped samples. The dominant emission signals for OSL and TSL are 5d → 4f transitions of the Ce^{3+}. The Ce^{3+} content in CMS affects photochromic efficiency, OSL decay, TSL intensity, and charge trap distribution. The results indicate that CMS: 0.1% has the highest potential for dosimetric applications due to the highest TSL intensity of deep charge traps and the fastest OSL decay.

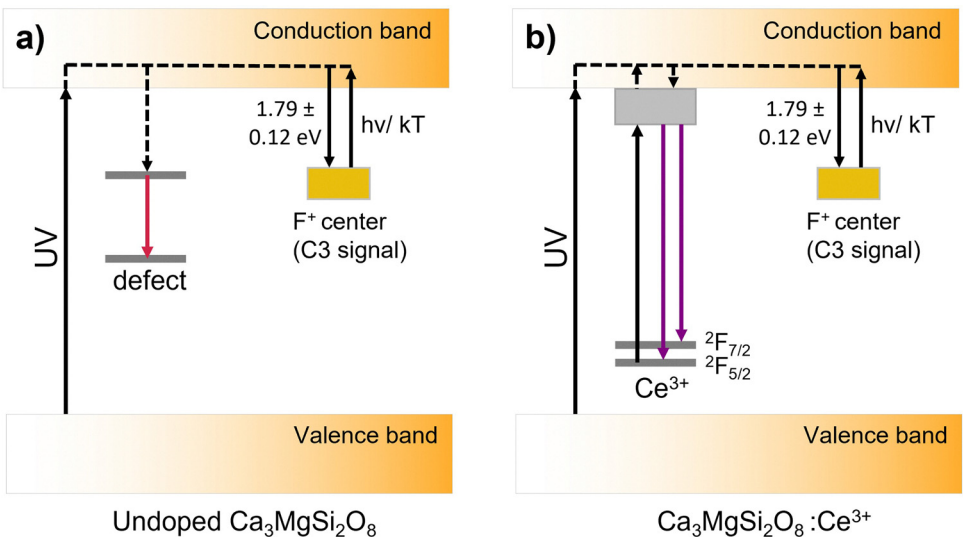

Fig. 11 Schematic energy level diagram of (a) undoped $Ca_3MgSi_2O_8$ and (b) $Ca_3MgSi_2O_8$:Ce^{3+}.

4. Conclusions

A novel photochromic material, $Ca_3MgSi_2O_8:Ce^{3+}$, with exceptionally high color contrast, an efficient OSL signal, and a linear TSL dose response up to 40 Gy, has been developed. XANES studies indicate that the oxidation state of cerium ions in the $Ca_3MgSi_2O_8$ lattice is predominantly 3+, whereas the EXAFS analysis suggests that cerium mainly substitutes at Ca2 sites in a distorted eightfold coordination. Variations in Ce^{3+} concentration affect the charge trap distribution and the overall contribution of different defect-related signals in the TSL, EPR, and diffuse reflectance spectra. Ce^{3+} doping also improves the recombination processes in $Ca_3MgSi_2O_8$, likely by participating in charge trapping during the excitation. EPR data indicate the presence of three distinct F^+ centers with different stabilities in the investigated material. The comparison of the spectroscopic data indicates that the dominant TSL and photochromic signals are associated with the F^+ center with the highest thermal stability (C3). The combination of excellent stability with efficient spectroscopic properties suggests that $Ca_3MgSi_2O_8:Ce^{3+}$ is a promising material for dosimetry applications.

Conflicts of interest

There are no conflicts to declare.

Data availability

The code XAESA for the analysis of extended X-ray absorption fine structure (EXAFS) spectra can be found at https://gitlab.desy.de/aleksandr.kalinko/xaesa.

The thermostimulated luminescence, photoluminescence, electron paramagnetic resonance and diffuse reflectance data supporting this study have been included within the article and the corresponding supplementary information (SI). Supplementary information is available. See DOI: https://doi.org/10.1039/d6tc00316h.

Acknowledgements

This project has received funding from the Research Council of Lithuania (LMTLT), agreement No. S-PD-24-67. We acknowledge DESY (Hamburg, Germany), a member of the Helmholtz Association HGF, for the provision of experimental facilities.

References

1 D. Li, X. Zheng, H. He, P. Boutinaud, S. Xiao, J. Xu, C. Wang, Y. Hu and F. Kang, A 20-Year Review of Inorganic Photochromic Materials: Design Consideration, Synthesis Methods, Classifications, Optical Properties, Mechanism Models, and Emerging Applications, *Laser Photon. Rev.*, 2024, **18**, 2400742, DOI: 10.1002/lpor.202400742.

2 J. Du, Z. Yang, H. Lin and D. Poelman, Inorganic photochromic materials: Recent advances, mechanism, and emerging applications, *Responsive Mater.*, 2024, **2**, e20240004, DOI: 10.1002/rpm.20240004.

3 J. Zou, J. Liao, Y. He, T. Zhang, Y. Xiao, H. Wang, M. Shen, T. Yu and W. Huang, Recent Development of Photochromic Polymer Systems: Mechanism, Materials, and Applications, *Research*, 2024, **7**, 0392, DOI: 10.34133/research.0392.

4 Z. Yang, J. Du, L. I. D. J. Martin, A. Feng, E. Cosaert, B. Zhao, W. Liu, R. Van Deun, H. Vrielinck and D. Poelman, Designing Photochromic Materials with Large Luminescence Modulation and Strong Photochromic Efficiency for Dual-Mode Rewritable Optical Storage, *Adv. Opt. Mater.*, 2021, **9**, 2100669, DOI: 10.1002/ADOM.202100669.

5 R. Zhang, Y. Jin, C. Wang, H. Wu, L. Chen and Y. Hu, A photochromic material-based platform for high-precision UV light detection and erasable optical information storage, *J. Alloys Compd.*, 2023, **934**, 167918, DOI: 10.1016/j.jallcom.2022.167918.

6 H. C. Byron, C. Swain, P. Paturi, P. Colinet, R. Rullan, V. Halava, T. Le Bahers and M. Lastusaari, Highly Tuneable Photochromic Sodalites for Dosimetry, Security Marking and Imaging, *Adv. Funct. Mater.*, 2023, **33**, 2303398, DOI: 10.1002/adfm.202303398.

7 Z. Yang, J. Hu, D. Van der Heggen, M. Jiao, A. Feng, H. Vrielinck, P. F. Smet, D. Poelman and A. Versatile, Photochromic Dosimeter Enabling Detection of X-Ray, Ultraviolet, and Visible Photons, *Laser Photon. Rev.*, 2023, **17**, 2200809, DOI: 10.1002/LPOR.202200809.

8 W. Meng, J. Wang and L. Jiang, Recent advances in photochromic smart windows based on inorganic materials, *Adv. Opt. Mater.*, 2024, **2**, e20240001, DOI: 10.1002/rpm.20240001.

9 L. Österlund, J. Montero and G. A. Niklasson, Inorganic Thermochromics and Photochromics, *Chromogenics*, Wiley, 2026, pp. 293–340, DOI: 10.1002/9781394159109.ch7.

10 M. Liu, J. Shao, X. Li, Y. Guo, C. Lu, S. Ke, H. Sun and Q. Zhang, BaMgSiO4-based composites with photochromic and persistent luminescent behaviors for advanced anti-counterfeiting applications, *Ceram. Int.*, 2025, **51**, 21735–21741, DOI: 10.1016/j.ceramint.2025.02.334.

11 J. Hu, B. Duan, J. Yao, T. Luo, Y. Wu, F. Wang, T. Liu, C. Ding, Q. Fan and H. Fu, Multimodal anti-counterfeiting and optical storage application based on luminescence reversible modification and color change of photochromic phosphor, *Appl. Mater. Today*, 2024, **40**, 102392, DOI: 10.1016/j.apmt.2024.102392.

12 M. Akiyama, H. Yamada and K. Sakai, Photochromism enhancement in reduced tridymite BaMgSiO4 by Fe-doping, *J. Ceram. Soc. Jpn.*, 2011, **119**, 338–341, DOI: 10.2109/jcersj2.119.338.

13 W. Tang, C. Zuo, C. Ma, Y. Wang, Y. Li, X. Yuan, E. Wang, Z. Wen and Y. Cao, Designing photochromic materials with high photochromic contrast and large luminescence modulation for hand-rewritable information displays and dual-mode optical storage, *Chem. Eng. J.*, 2022, **435**, 134670, DOI: 10.1016/j.cej.2022.134670.

14 S. Kamimura, H. Yamada and C.-N. Xu, Purple photochromism in $Sr_2SnO_4:Eu^{3+}$ with layered perovskite-related

structure, *Appl. Phys. Lett.*, 2013, **102**, 31110, DOI: 10.1063/1.4788752.

15 G. Ju, Y. Hu, L. Chen and X. Wang, Photochromism of rare earth doped barium haloapatite, *J. Photochem. Photobiol. A Chem.*, 2013, **251**, 100–105, DOI: 10.1016/j.jphotochem.2012.10.021.

16 A. V. Egranov, T. Y. Sizova, N. A. R.Yu. Shendrik and Smirnova, Instability of some divalent rare earth ions and photochromic effect, *J. Phys. Chem. Solids*, 2016, **90**, 7–15, DOI: 10.1016/j.jpcs.2015.11.007.

17 G. Okada, T. Kato, D. Nakauchi, K. Fukuda and T. Yanagida, Photochromism and Thermally and Optically Stimulated Luminescences of AlN Ceramic Plate for UV Sensing, *Sens. Mater.*, 2016, **28**, 897–904.

18 R. Yang, L. Chen, C. Lin, H. Huang, Z. Wu, C. Zhan, Y. Zhuang and R.-J. Xie, Relationship between photochromism and persistent luminescence in barium-magnesium silicates, *Chem. Eng. J.*, 2024, **493**, 152578, DOI: 10.1016/j.cej.2024.152578.

19 L. Sun, B. Wang, G. Xing, C. Liang, W. Ma and S. Yang, Bi-induced photochromism and photo-stimulated luminescence with fast photochromic response for multi-mode dynamic anti-counterfeiting and optical information storage, *Chem. Eng. J.*, 2023, **455**, 140752, DOI: 10.1016/J.CEJ.2022.140752.

20 R. Cao, N. Liu, Q. Zhong, Y. Tu, Y. Xu, H. Zhang, W. Luo and T. Chen, Luminescence properties and tunable emission of $Ca_3MgSi_2O_8$:Eu^{3+}, Bi^{3+} phosphor with $Bi^{3+} \rightarrow Eu^{3+}$ energy transfer, *J. Mater. Sci.: Mater. Electron.*, 2021, **32**, 26620–26630, DOI: 10.1007/s10854-021-07039-2.

21 R. Cao, Y. Zheng, T. Chen, B. Lan, L. Li, Q. Zhong, S. Nie and J. Wang, Synthesis and tunable emission from yellow-green to red-orange of $Ca_3MgSi_2O_8$:Eu^{3+}, Dy^{3+} phosphor, *J. Mol. Struct.*, 2022, **1262**, 133008, DOI: 10.1016/j.molstruc.2022.133008.

22 N. S. Kuriyan, P. S. Ghosh, M. Parvathy and A. Arya, Unraveling the role of crystal structural variations in modifying the luminescence properties of CMS: Eu^{3+} phosphor, *J. Lumin.*, 2025, **277**, 120894, DOI: 10.1016/j.jlumin.2024.120894.

23 Y. Lin, Z. Tang, Z. Zhang and C. W. Nan, Luminescence of Eu^{2+} and Dy^{3+} activated $R_3MgSi_2O_8$-based (R = Ca, Sr, Ba) phosphors, *J. Alloys Compd.*, 2003, **348**, 76–79, DOI: 10.1016/S0925-8388(02)00796-X.

24 Y. Chen, X. Cheng, M. Liu, Z. Qi and C. Shi, Comparison study of the luminescent properties of the white-light long afterglow phosphors: $CaxMgSi_2O_5$ + x:Dy^{3+} (x = 1, 2, 3), *J. Lumin.*, 2009, **129**, 531–535, DOI: 10.1016/j.jlumin.2008.12.008.

25 Y. Lin, Z. Zhang, Z. Tang, X. Wang, J. Zhang and Z. Zheng, Luminescent properties of a new long afterglow Eu^{2+} and Dy^{3+} activated $Ca_3MgSi_2O_8$ phosphor, *J. Eur.*, 2001, **21**, 683–685, DOI: 10.1016/S0955-2219(00)00252-1.

26 P. Dewangan, D. P. Bisen, N. Brahme and S. Sharma, Structural characterization and luminescence properties of Dy^{3+} doped $Ca_3MgSi_2O_8$ phosphors, *J. Alloys Compd.*, 2019, **777**, 423–433, DOI: 10.1016/j.jallcom.2018.10.390.

27 G. Krieke, A. Antuzevics, G. Doke, A. Kareiva and A. Zarkov, Tunable Highly Efficient Photochromism and Multimodal Luminescence in $(Ca,Sr)_3MgSi_2O_8$:Eu^{2+} Solid Solutions, *ACS Appl. Opt. Mater.*, 2025, **3**, 2173–2183, DOI: 10.1021/acsaom.5c00275.

28 G. Krieke, A. Antuzevics, A. Kalinko, A. Kuzmin, T. Murauskas, A. Kareiva and A. Zarkov, Matrix-dependent high-contrast photochromism in Eu-doped $M_3MgSi_2O_8$ (M = Ca, Sr, Ba), *J. Mater. Chem. C*, 2024, **12**, 16989–16998, DOI: 10.1039/D4TC03091E.

29 D. Jia, R. S. Meltzer and W. M. Yen, Ce^{3+} energy levels relative to the band structure in CaS: evidence from photoionization and electron trapping, *J. Lumin.*, 2002, **99**, 1–6, DOI: 10.1016/S0022-2313(02)00326-5.

30 M. Kitaura, H. Zen, S. Watanabe, H. Masai, K. Kamada, K.-J. Kim, A. Yoshikawa and J. Ueda, Relationship between Ce^{3+} 5d1 level, conduction-band bottom, and shallow electron trap level in $Gd_3Ga_5O_{12}$:Ce and $Gd_3Al_1Ga_4O_{12}$:Ce crystals studied via pump-probe absorption spectroscopy, *Opt. Mater.:X*, 2025, **25**, 100398, DOI: 10.1016/j.omx.2024.100398.

31 V. Laguta, L. Havlak, V. Babin, J. Barta, J. Pejchal and M. Nikl, Charge Transfer and Charge Trapping Processes in Ca- or Al-Co-doped Lu_2SiO_5 and $Lu_2Si_2O_7$ Scintillators Activated by Pr^{3+} or Ce^{3+} Ions, *Materials*, 2023, **16**, 4488, DOI: 10.3390/ma16124488.

32 N. V. Znamenskii, E. A. Manykin, E. A. Petrenko, T. G. Yukina, Yu. V. Malyukin, P. N. Zhmurin, B. V. Grinev, A. A. Masalov and A. P. Shpak, The nature and mechanism of charging of electron traps in Lu_2SiO_5:Ce^{3+} crystals, *J. Exp. Theor. Phys.*, 2004, **99**, 386–393, DOI: 10.1134/1.1800196.

33 W. A. Caliebe, V. Murzin, A. Kalinko and M. Görlitz, High-flux XAFS-beamline P64 at PETRA III, *AIP Conf. Proc.*, 2019, **2054**, 060031, DOI: 10.1063/1.5084662.

34 A. Kalinko, XAESA, (2023). https://gitlab.desy.de/aleksandr.kalinko/xaesa (accessed January 22, 2026).

35 A. Kuzmin and J. Chaboy, EXAFS and XANES analysis of oxides at the nanoscale, *IUCrJ*, 2014, **1**, 571–589, DOI: 10.1107/S2052252514021101.

36 A. L. Ankudinov, B. Ravel, J. J. Rehr and S. D. Conradson, Real-space multiple-scattering calculation and interpretation of x-ray-absorption near-edge structure, *Phys. Rev. B:Condens. Matter Mater. Phys.*, 1998, **58**, 7565–7576, DOI: 10.1103/PhysRevB.58.7565.

37 L. Hedin and B. I. Lundqvist, Explicit local exchange-correlation potentials, *J. Phys. C: Solid State Phys.*, 1971, **4**, 2064–2083, DOI: 10.1088/0022-3719/4/14/022.

38 Y. Yonesaki, T. Takei, N. Kumada and N. Kinomura, Crystal structure of Eu^{2+} -doped $M_3MgSi_2O_8$ (M: Ba, Sr, Ca) compounds and their emission properties, *J. Solid State Chem.*, 2009, **182**, 547–554, DOI: 10.1016/j.jssc.2008.11.032.

39 S. Stoll and A. Schweiger, EasySpin, a comprehensive software package for spectral simulation and analysis in EPR, *J. Magn. Reson.*, 2006, **178**, 42–55.

40 R. D. Shannon and C. T. Prewitt, Revised values of effective ionic radii, *Acta Crystallogr., Sect. B*, 1970, **26**, 1046–1048, DOI: 10.1107/S0567740870003576.

41 J. Ueda and S. Tanabe, Review of luminescent properties of Ce^{3+} -doped garnet phosphors: New insight into the effect of crystal and electronic structure, *Opt. Mater.:X*, 2019, **1**, 100018, DOI: 10.1016/j.omx.2019.100018.
42 B. Wang, Y. Liu, Z. Huang and M. Fang, Photoluminescence properties of a Ce^{3+} doped $Sr_3MgSi_2O_8$ phosphor with good thermal stability, *RSC Adv.*, 2018, **8**, 15587–15594, DOI: 10.1039/C8RA00526E.
43 H. Lihui, Z. Xiao and L. Xingren, Studies on luminescence properties and crystallographic sites of Ce^{3+} in $Ca_3MgSi_2O_8$, *J. Alloys Compd.*, 2000, **305**, 14–16, DOI: 10.1016/S0925-8388(00)00734-9.
44 P. Dorenbos, 5d-level energies of Ce^{3+} and the crystalline environment. IV. Aluminates and "simple" oxides, *J. Lumin.*, 2002, **99**, 283–299, DOI: 10.1016/S0022-2313(02)00347-2.
45 A. Bianconi, A. Marcelli, H. Dexpert, R. Karnatak, A. Kotani, T. Jo and J. Petiau, Specific intermediate-valence state of insulating 4f compounds detected by L3 x-ray absorption, *Phys. Rev. B:Condens. Matter Mater. Phys.*, 1987, **35**, 806–812, DOI: 10.1103/PhysRevB.35.806.
46 E. Kaewnuam, N. Wantana, Y. Ruangtaweep, M. Cadatal-Raduban, K. Yamanoi, H. J. Kim, P. Kidkhunthod and J. Kaewkhao, The influence of CeF_3 on radiation hardness and luminescence properties of Gd_2O_3–B_2O_3 glass scintillator, *Sci. Rep.*, 2022, **12**, 11059, DOI: 10.1038/s41598-022-14833-3.
47 K. O. Kvashnina, Electronic-Structure Interpretation: How Much Do We Understand Ce L3 XANES?, *Chem. – Eur. J.*, 2024, **30**, e202400755, DOI: 10.1002/chem.202400755.
48 A. V. Soldatov, T. S. Ivanchenko, S. Della Longa, A. Kotani, Y. Iwamoto and A. Bianconi, Crystal-structure effects in the Ce L3 -edge x-ray-absorption spectrum of CeO_2: Multiple-scattering resonances and many-body final states, *Phys. Rev. B:Condens. Matter Mater. Phys.*, 1994, **50**, 5074–5080, DOI: 10.1103/PhysRevB.50.5074.
49 A. J. J. Bos, Theory of thermoluminescence, *Radiat. Meas.*, 2006, **41**(1), S45–S56, DOI: 10.1016/j.radmeas.2007.01.003.
50 A. J. J. Bos, Thermoluminescence as a research tool to investigate luminescence mechanisms, *Materials*, 2017, **10**(12), 1357, DOI: 10.3390/ma10121357.
51 E. G. Yukihara, A. C. Coleman, R. H. Biswas, R. Lambert, F. Herman and G. E. King, Thermoluminescence analysis for particle temperature sensing and thermochronometry: Principles and fundamental challenges, *Radiat. Meas.*, 2018, **120**, 274–280, DOI: 10.1016/j.radmeas.2018.05.007.
52 G. Doke, G. Krieke, P. Rodionovs, D. Nilova and A. Antuzevics, Trap properties of a novel UV-A persistent phosphor $Sr_3MgSi_2O_8$:Ce^{3+}, *J. Rare Earths*, 2025, **43**, 676–683, DOI: 10.1016/j.jre.2024.03.008.
53 Y. Kitagawa, J. Ueda and S. Tanabe, Blue Persistent Phosphor of $YSiO_2N$:Ce^{3+} Developed by Codoping Sm^{3+} or Tm^{3+} Ions and Thermoluminescence Analysis of Their Trap Distributions, *Phys. Status Solidi A*, 2022, **219**(5), 2100670, DOI: 10.1002/pssa.202100670.
54 A. Dobrowolska, A. J. J. Bos and P. Dorenbos, Electron tunnelling phenomena in YPO_4:Ce,Ln (Ln = Er, Ho, Nd, Dy), *J. Phys. D: Appl. Phys.*, 2014, **47**, 335301, DOI: 10.1088/0022-3727/47/33/335301.
55 M. Kitaura, A. Sato, K. Kamada, A. Ohnishi and M. Sasaki, Phosphorescence of Ce-doped $Gd_3Al_2Ga_3O_{12}$ crystals studied using luminescence spectroscopy, *J. Appl. Phys.*, 2014, **115**(8), 083517, DOI: 10.1063/1.4867315.
56 A. Vedda, M. Nikl, M. Fasoli, E. Mihokova, J. Pejchal, M. Dusek, G. Ren, C. R. Stanek, K. J. McClellan and D. D. Byler, Thermally stimulated tunneling in rare-earth-doped oxyorthosilicates, *Phys. Rev. B: Condens. Matter Mater. Phys.*, 2008, **78**(19), 195123, DOI: 10.1103/PhysRevB.78.195123.
57 S. Akca, M. Oglakci, Z. G. Portakal, N. Kucuk, M. Bakr, M. Topaksu and N. Can, Thermoluminescence analysis of beta irradiated ZnB_2O_4:Pr^{3+} phosphors synthesized by a wet-chemical method, *Radiat. Phys. Chem.*, 2019, **160**, 105–111, DOI: 10.1016/j.radphyschem.2019.03.033.
58 K. H. Gavhane, M. S. Bhadane, A. S. Bhoir, P. P. Kulkarni, B. J. Patil, V. N. Bhoraskar, S. D. Dhole and S. S. Dahiwale, T_m-T_{stop} analysis and dosimetric properties of Ce doped BaB_4O_7 phosphor, *J. Alloys Compd.*, 2020, **817**, 152805, DOI: 10.1016/j.jallcom.2019.152805.
59 S. Pazylbek, J. Stadulis, G. Doke, A. Antuzevics, V. Pankratov, G. Merkininkaite, A. Katelnikovas and A. Zarkov, Tunable broadband visible emission achieved by phase transformation-driven self-reduction of Eu^{3+} to Eu^{2+} in a calcium phosphate matrix, *Dalton Trans.*, 2025, **54**, 8625–8634, DOI: 10.1039/d5dt00681c.
60 Y. S. Horowitz, Theory of thermoluminescence gamma dose response: The unified interaction model, *Nucl. Instrum. Methods Phys. Res., Sect. B*, 2001, **184**, 68–84, DOI: 10.1016/S0168-583X(01)00712-1.
61 S. F. Kry, P. Alvarez, J. E. Cygler, L. A. DeWerd, R. M. Howell, S. Meeks, J. O'Daniel, C. Reft, G. Sawakuchi, E. G. Yukihara and D. Mihailidis, AAPM TG 191: Clinical use of luminescent dosimeters: TLDs and OSLDs, *Med. Phys.*, 2020, **47**, e19–e51, DOI: 10.1002/mp.13839.
62 J. A. Weil and J. R. Bolton, *Electron Paramagnetic Resonance*, Wiley, 2007.
63 M. P. Scripsick, X. H. Fang, G. J. Edwards, L. E. Halliburton and J. K. Tyminski, Point defects in lithium triborate (LiB_3O_5) crystals, *J. Appl. Phys.*, 1993, **73**, 1114–1118, DOI: 10.1063/1.353275.
64 W. Hong, L. E. Halliburton, K. T. Stevens, D. Perlov, G. C. Catella, R. K. Route and R. S. Feigelson, Electron paramagnetic resonance study of electron and hole traps in β-BaB_2O_4 crystals, *J. Appl. Phys.*, 2003, **94**, 2510–2515, DOI: 10.1063/1.1590051.
65 M. W. Swinney, J. W. McClory, J. C. Petrosky, S. Yang, A. T. Brant, V. T. Adamiv, Ya. V. Burak, P. A. Dowben and L. E. Halliburton, Identification of electron and hole traps in lithium tetraborate ($Li_2B_4O_7$) crystals: Oxygen vacancies and lithium vacancies, *J. Appl. Phys.*, 2010, **107**(11), 113715, DOI: 10.1063/1.3392802.
66 B. C. Holloway, C. A. Lenyk, T. D. Gustafson, N. C. Giles, D. Perlov and L. E. Halliburton, Oxygen vacancies in LiB_3O_5 crystals and their role in nonlinear absorption, *Opt. Mater. Express*, 2022, **12**, 4155, DOI: 10.1364/OME.469756.

